



# Effects of blade aspect ratio and taper ratio on hovering performance of cycloidal rotor with large blade pitching amplitude



Yu HU \*, Xuyang FU, Hailang ZHANG, Gengqi WANG, Hussain FARHAT

School of Aeronautics, Northwestern Polytechnical University, Xi'an 710072, China

Received 28 March 2018; revised 29 July 2018; accepted 20 September 2018  
Available online 8 February 2019

## KEYWORDS

Blade pitching motion;  
Cyclocopter;  
Cyclogyro;  
Cycloidal rotor;  
Dynamic stall

**Abstract** In recent years, a lot of research work has been carried out on the cycloidal rotors. However, it lacks thorough understanding about the effects of the blade platform shape on the hover efficiency of the cycloidal rotor, and the knowledge of how to design the platform shape of the blades. This paper presents a numerical simulation model based on Unsteady Reynolds-Averaged Navier-Stokes equations (URANSs), which is further validated by the experimental results. The effects of blade aspect ratio and taper ratio are analyzed, which shows that the cycloidal rotors with the same chord length have quite similar performance even though the blade aspect ratio varies from a very small value to a large one. By comparing the cycloidal rotors with different taper ratios, it is found that the rotors with large blade taper ratio outperform those with small taper ratio. This is due to the fact that the blade with larger taper ratio has longer chord and hence better efficiency. The analysis results show that the unsteady aerodynamic effects due to blade pitching motion play a more important role in the efficiency than the blade platform shape. Therefore we should pay more attention to the blade airfoil and pitching motion than the blade platform shape. The main contributions of this paper include: the analysis of the effects of aspect ratio and taper ratio on the hover efficiency of cycloidal rotor based on both the experimental and numerical simulation results; the finding of the main influencing factors on the hover efficiency; the qualitative guidance on how to design the blade platform shape for cycloidal rotors.

© 2019 Chinese Society of Aeronautics and Astronautics. Production and hosting by Elsevier Ltd. This is an open access article under the CC BY-NC-ND license (<http://creativecommons.org/licenses/by-nc-nd/4.0/>).

## 1. Introduction

Cycloidal rotor is a type of propeller whose blades rotate around an axis in parallel with the rotor shaft. The dynamic pitching of the blades generates thrust due to unsteady aerodynamic effects. The aircraft that flies by cycloidal rotors is called a cyclogyro or cyclocopter. For the cycloidal rotors with large pitching amplitude, the Dynamic Stall Vortices (DSVs)

\* Corresponding author.

E-mail address: [Julius\\_hu@hotmail.com](mailto:Julius_hu@hotmail.com) (Y. HU).

Peer review under responsibility of Editorial Committee of CJA.



produced by blade pitching motion will induce Blade Vortex Interactions (BVIs) upon neighboring blades.<sup>1</sup> Since the blade is actually pitching in the curvilinear flow, the virtual camber and virtual incidence effects caused by the flow curvature have a significant impact on the performance of the cycloidal rotor.<sup>2,3</sup>

The cycloidal rotor incorporates potentially high aerodynamic efficiency, very low noise and vectored thrust at low Reynolds number, and it could be a good propulsion device for Micro Air Vehicles (MAVs) that flies in confined space.<sup>2,3</sup> In recent years, due to its potential benefits, the cycloidal rotor has attracted the researchers. Iosilevskii and Levy carried out the numerical studies on the cycloidal rotor with diameter of 0.11 m.<sup>4</sup> They found that the stream traces around the rotor formed a distorted doublet. The Fast Fourier Transformation (FFT) analysis was performed on rotor force history. It is found that there are intense interactions among the blades. Hwang et al. developed several cyclocopters. The test flights proved that it is possible to maintain the stable and controlled flight with the help of cycloidal rotors.<sup>5-7</sup> Lee et al. developed a cyclocopter with two cycloidal rotors and one tail rotor. They developed a novel analytic aerodynamic model for the cycloidal rotors. Finally a hovering flight was performed in a tethered test.<sup>8</sup> Benedict et al.<sup>9-11</sup> also performed extensive researches on the cycloidal rotors based on experiments and numerical simulations. Based on experimental approach, the cycloidal rotors with different design parameters were discussed by parametric analysis. They concluded that the cycloidal rotor has higher hover efficiency than screw rotor and the elastic torsion of the blade structure can result in smaller aerodynamic force.<sup>2</sup> They also developed remote controlled cyclocopter that flied with good stability.<sup>12,13</sup> Yang integrated the aero-elastic model into the OVERFLOW and performed numerical simulations with cycloidal propellers. The analysis indicates that both 2D and 3D analysis can produce results that are quite close to the experimental results.<sup>14</sup> Leger et al. developed a simulation model for the cycloidal rotor with good accuracy.<sup>15</sup> Xisto et al. performed parametric analysis on the cycloidal propeller in hover status.<sup>16</sup> They concluded that the best chord to radius ratio is about 0.5 and the best pitching axis location is 35% of blade chord from the leading edge. Gagnon et al. developed the analytical model for the cycloidal rotors. The analyses suggest that cycloidal rotors can increase the efficiency of a helicopter at high velocities while flexibility reduces it and may lead to instabilities.<sup>17</sup> The 2D and 3D numerical simulations were performed by us to study the aerodynamics of the cycloidal rotors.<sup>1,18</sup> The analysis results indicate that Unsteady Reynolds-Averaged Navier-Stokes equations (URANSs) are adequate to predict the details of the aerodynamic forces and flow field of the cycloidal rotor with affordable computation resources. 2D model can predict the aerodynamic forces well even though the Blade Tip Vortices (BTVs) are absent.<sup>1,18</sup>

Although the effects of the blade platform shape had been studied based on parametric analysis,<sup>9,10</sup> it still lacks thorough understanding about the effects of the blade platform shape on the hover efficiency of the cycloidal rotor and the knowledge of how to design the blade platform shape.

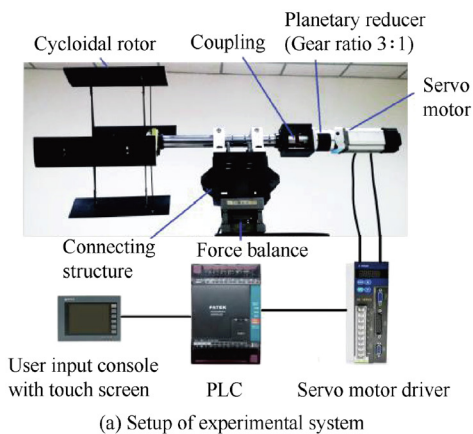
In this paper, 2D and 3D numerical simulation models for cycloidal rotors are developed to study the effects of blade aspect ratio and taper ratio. Based on the numerical simulation results, the details of the flow field and rotor force production

history are also discussed. Then a qualitative perspective on how to design the blade platform shape of the cycloidal rotors is presented.

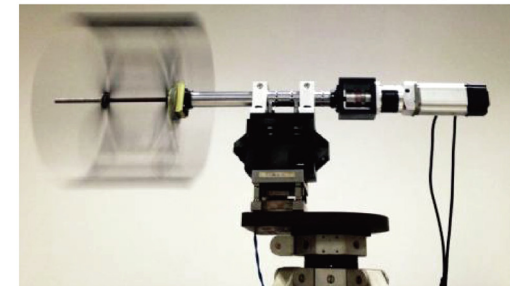
## 2. Force measurement of cycloidal rotor

The aerodynamic forces of the cycloidal rotor are measured by experiments in order to validate the numerical simulation model. The experimental apparatus is shown in Fig. 1. The parameters of the cycloidal rotor are shown in Table 1.

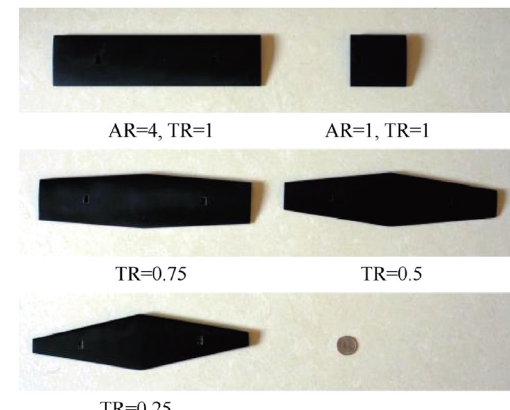
The blade skin is made of carbon fiber sheet and the blade spar is a carbon fiber tube. The rotor is powered by a Panasonic servo motor rated at 600 W. The rotation speed can be controlled precisely by the servo motor driver. The user can control the servo motor through a Liquid Crystal Display (LCD) touch screen console. A Programmable Logic Con-



(a) Setup of experimental system



(b) Cycloidal rotor in operation



(c) Blades with different Aspect Ratios (AR) and Taper Ratios (TR)

**Fig. 1** Experimental apparatus.

<b>Table 1</b> Parameters of baseline cycloidal rotor in experiments.	
Parameter	Value
Rotor diameter (mm)	360
Number of blades	4
Chord length (mm)	70
Blade aspect ratio	4
Airfoil of blade	NACA0015
Blade pitch axis position	50% chord length from leading edge
Pitch angle amplitude (°)	45

troller (PLC) then converts and feeds the user command into the servo motor driver, as shown in Fig. 1 (a). The forces from the cycloidal rotor are measured by a 6-component force balance manufactured by China Aerodynamic Research and Development Center. The static error of the force balance is less than or equal to 0.3%. The excitation power for the force balance is 11 V with accuracy of 50  $\mu$ V. The Data Conditioning And Acquisition (DCAQ) module consists of a NI SCXI-1520 and a NI PCI-6133 card.

The cycloidal rotors with different blade aspect ratios and taper ratios are also tested (Fig. 1(c)). The experiments not only provide the experimental data to exposit the effects of aspect ratio and taper ratio, but also testify the capabilities of the numerical simulation models when there is large variation of blade platform parameters.

### 3. Numerical simulation model of cycloidal rotor

#### 3.1. Selection of numerical simulation model

Several analysis models have been developed to predict the aerodynamic forces of the cycloidal rotors. These algorithms fall into three categories.

The first category is the semi-analytical and semi-empirical model. The analytic models for pitching airfoils (Theodorsen's theory or Garrick model, etc.) are usually employed to predict the aerodynamic forces due to blade pitching motion. The downwash in the rotor cage and interactions among the blades are then modeled by semi-empirical approaches. The 3D effects of the blades are usually predicted by the formulae of wing theory for fixed wing aircraft. McNabb developed an analysis model based on Theodorsen's theory for pitching airfoil. The downwash in the rotor cage was evaluated by the empirical equation for co-axial helicopter rotor.<sup>19</sup> Benedict et al. developed the double-multiple stream tube inflow model.<sup>2</sup> The rotor was divided into a number of stream tubes. The stream tubes intersected the rotor twice at the upstream and downstream intersection point. The blade swept area was deemed as thin actuator surfaces, across which the rotor imparts axial momentum into the flow.<sup>2</sup> Leger et al. proposed the equivalent rotor model.<sup>15,16</sup> In this model, the blade oscillation was simulated by Garrick model. The resultant velocity of blade was computed by the empirical equations.

The second category is based on potential flow theories. An unsteady free wake model was developed by Tang et al.<sup>20</sup> This approach was performed by the combination of stream-tube inflow model, lifting-line formulation, free wake model and the semi-empirical Leishman-Beddoes (L-B) dynamic stall model. The initial flow field was given by stream-tube inflow

model, and then the aerodynamic force and effects of wake were predicted by lifting-line theory. The lift and drag of the blade elements were predicted by the L-B dynamic stall model. This model is limited to the blades with large aspect ratio because of lifting-line formulation.<sup>21</sup> Prabhu et al. developed a 2D numerical model based on panel method. The surface of the airfoil was discretized into a number of panels. A point vortex was shed tangential to the trailing edge of the blade at each time step. The strength of the free vortex was equal to the change in the bound vortex but was opposite in sign.<sup>22</sup> The free vortices convect with local velocity at each time step.

The last category is based on the CFD approach, where the Unsteady Reynolds-Averaged Navier-Stokes Equations (URANS) is solved. This approach has been widely used in dynamic stall simulation and analysis.<sup>12</sup> Yang performed the numerical simulation based on URANS and overset mesh technique using OVERTURNS.<sup>14</sup> The CFD simulation results show that the simulation based on 2D mesh system corresponds to the mid-span section of the 3D mesh system. Both the 2D and 3D simulation can obtain fairly good prediction of the vertical force, but cannot capture side force well, and thus underestimate the power. Both 2D and 3D simulation can produce fairly good flow field compared with results from Particle Image Velocimetry (PIV) experiments. Legar et al. performed 2D CFD analysis based on a finite-volume implementation of the incompressible URANS. The numerical simulation can provide satisfactory solutions in the presence of adverse pressure gradients and dynamic stall.<sup>16</sup> Gagnon proposed the 3D numerical simulations based on sliding mesh technique using OpenFOAM.<sup>17</sup>

All the models stated above can predict the aerodynamic forces with good accuracy. However, the semi-empirical models are based on certain assumptions and simplifications. The details of the physics lying behind the cycloidal rotors are neglected. Sometimes there are certain semi-empirical parameters deduced from the experimental results, making these models highly case specific. They are not suitable for parametric study if vast variation of design parameters was involved. The models based on potential flow theories are also based on certain assumptions or simplifications. These models have difficulties in simulating the behavior of DSVs and blade vortex interactions. The CFD approaches can produce not only good predictions of the forces of the cycloidal rotors, but also the details of the flow field that are validated by the PIV experiments. For the test cases to be discussed in this paper, there is large variation of design parameters regarding the blade platform shape. To study the mechanisms of the cycloidal rotors, the analysis on the details of the flow field is needed. Therefore the numerical simulation model based on incompressible URANS and sliding mesh technique is selected in this paper.

#### 3.2. Blade pitching kinetics

The pitching control mechanism is shown in Fig. 2. The pitch angle of the blade is controlled by an eccentric. For the blade with pitch link fixed on the eccentric, the control mechanism is a four-bar control mechanism ( $O O' B A$ ). For the rest of blades with pitch link connected to the eccentric with hinge, the control mechanism is equivalent to the geared five-bar control mechanism with gear ratio of 1:1 ( $O O' C D E$ ), as shown in Fig. 2. The kinetics of the blades is expressed by

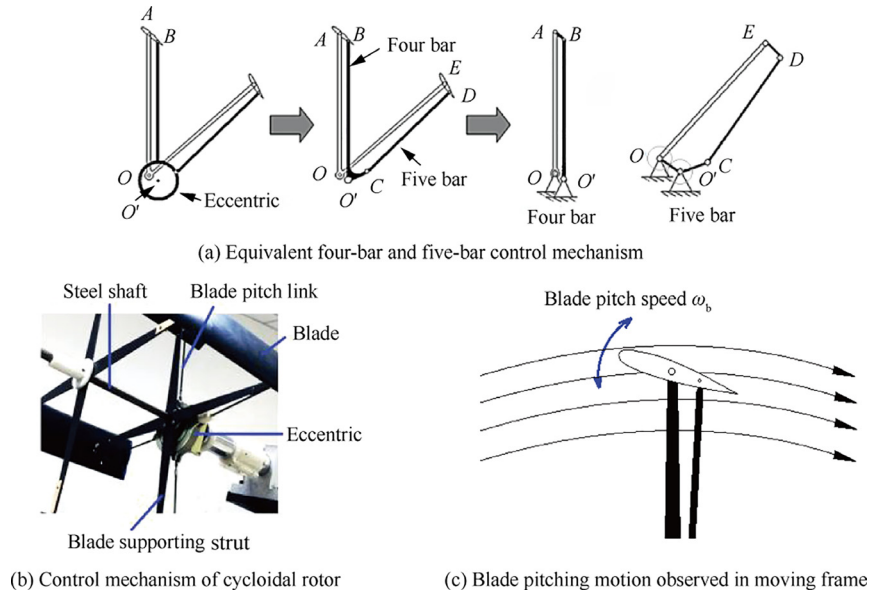


**Fig. 2** Kinetics of blade.

the equations for four-bar and geared five-bar mechanism with gear ratio of 1:1.<sup>23</sup> Equations for blade kinetics are then incorporated into the User Defined Functions (UDF) and loaded into the Fluent solver. As shown in Fig. 2 (c), if viewed in the moving frame that is attached to the blade supporting strut, the blade is actually performing pitching oscillation in the curvilinear flow.

### 3.3. Solver setup

The baseline design of the test cases to be discussed is defined in Table 1. All simulations are performed by ANSYS Fluent. The maximum blade peripheral velocity is 16.9 m/s, which falls into low speed range, and therefore the incompressible Navier–Stokes equations and the pressure based solver are employed. The Pressure Implicit with Splitting of Operators (PISO) scheme is selected to solve the pressure velocity coupling problem. The convective flux terms and the diffusive flux terms are discretized by second-order upwind scheme and second-order central difference scheme respectively. For the transient formulation, the second-order implicit time marching algorithm is selected. The incompressible Navier-Stokes equations solved in this paper are as follows:

$$\begin{aligned} \frac{\partial u}{\partial x} + \frac{\partial v}{\partial y} + \frac{\partial w}{\partial z} &= 0 \\ \rho \frac{du}{dt} &= S_{Mx} - \frac{\partial p}{\partial x} + \mu \left( \frac{\partial^2 u}{\partial x^2} + \frac{\partial^2 u}{\partial y^2} + \frac{\partial^2 u}{\partial z^2} \right) \\ \rho \frac{dv}{dt} &= S_{My} - \frac{\partial p}{\partial y} + \mu \left( \frac{\partial^2 v}{\partial x^2} + \frac{\partial^2 v}{\partial y^2} + \frac{\partial^2 v}{\partial z^2} \right) \\ \rho \frac{dw}{dt} &= S_{Mz} - \frac{\partial p}{\partial z} + \mu \left( \frac{\partial^2 w}{\partial x^2} + \frac{\partial^2 w}{\partial y^2} + \frac{\partial^2 w}{\partial z^2} \right) \end{aligned} \quad (1)$$

where  $\rho$  is density,  $p$  is pressure,  $t$  is time,  $(u, v, w)$  is velocity,  $\mu$  is viscosity coefficient and  $(S_{Mx}, S_{My}, S_{Mz})$  is source term.

### 3.4. Selection of turbulence model

There are three main types of turbulent modeling methods, i.e. Direct Numerical Simulation (DNS), Large Eddy Simulation

(LES) and Reynolds-Averaged Navier-Stokes (RANS). DNS is the most detailed approach, but it demands huge computation resources, and therefore it is too expensive to be used for the cases in this paper. LES is also too expensive to be used for such complex problems as discussed in this paper. According to the existing numerical simulation study on the dynamic stall, URANS is the best choice that incorporates both acceptable computation cost and accuracy.<sup>12,24–27</sup> The Reynolds number of the cycloidal rotor studied in this paper ranges from 20,000 to 80,000; hence the SST  $k-\omega$  model with low Reynolds correction is used. This model can predict the airfoil dynamic stall with better accuracy than that with the  $k-\epsilon$  model and the standard  $k-\omega$  model.<sup>12,24,25</sup>

### 3.5. Moving mesh techniques for cycloidal rotors

The motion of the blade can be decomposed into the revolution around the rotor shaft and the pitching oscillation about the pitching axis of the blade. To model the blade motion, the sliding mesh technique is employed.<sup>1,5</sup> Since the mesh elements of the sliding mesh need not to be deformed or re-meshed at each time step, the low quality elements due to mesh deformation or the time to update the mesh are avoided.<sup>13</sup>

As shown in Fig. 3, three levels of mesh blocks are deployed in the computation domain.<sup>1</sup> In this approach, a cylindrical hole is cut in the fixed mesh block (i.e. the fixed domain). The rotating mesh block around the cycloidal rotor, named as “revolving domain”, is fitted into that hole. The cylindrical hole for each blade is then cut in the “revolving domain”. The pitching mesh block around each blade, labeled as “pitching domain”, is fitted into the corresponding hole in the revolving domain. Mesh elements are condensed around the blade surface, the blade tip and the regions where the blade wake and vortices are expected. For all cases, the size of two adjacent mesh elements next to the mesh interfaces is carefully set, such that the ratio of their size is less than 2.0. This can reduce the influence of the hanging nodes, which cause discontinuities and spurious vortex structure.<sup>24</sup>

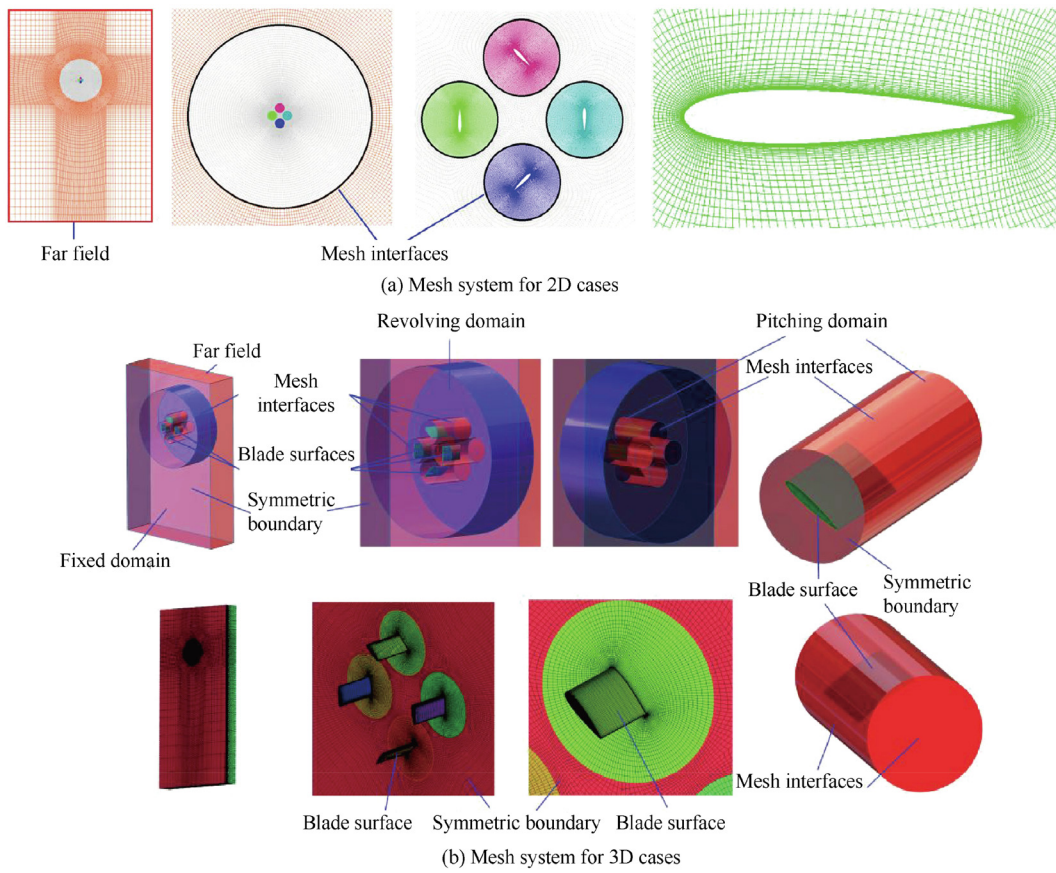


**Fig. 3** Mesh system for cycloidal rotors.

For all cases studied in this paper, the structured mesh is deployed in the whole computation domain. Only the cycloidal rotor with half blade span is modeled. There is a symmetric boundary (Fig. 3(b)) at the middle plane of the cycloidal rotor. In this way, the computation resources are cut down by half. The far field condition is set to be zero pressure gradients and zero velocity. In order to simulate the boundary layer effects more accurately, no wall function is used. Hence the height of the first row mesh near the blade surface is set such that  $y^+$  is equal to or less than 1. In the directions that are perpendicular to the rotor shaft, the far field stretches at least 20 times rotor diameter. In the direction that is parallel to the rotor shaft, the dimension of the computation domain

stretches at least 15 times blade span. This ensured that the influence of the far field is minimized.

The mesh independent tests are made as described in Ref.<sup>1</sup>. The results obtained by different mesh sizes are validated with experimental data. It is found that for each pitching domain around the blade, 240 mesh elements in the chord-wise direction, 104 grids in the span-wise direction and 54 grid elements in the radial direction are fine enough to generate mesh independent solution. There are about 1.2 million mesh elements for each pitching domain, more than 1 million mesh elements for the revolving domain and 500000 mesh elements for the fixed domain. Altogether there are about 6.5 million mesh elements in the computation domain. Various time step lengths

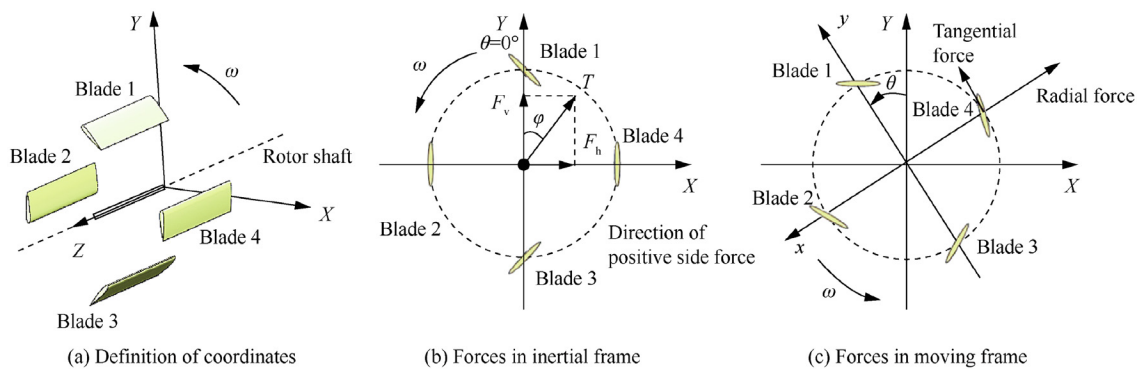


**Fig. 4** Definitions of reference frames and aerodynamic forces.

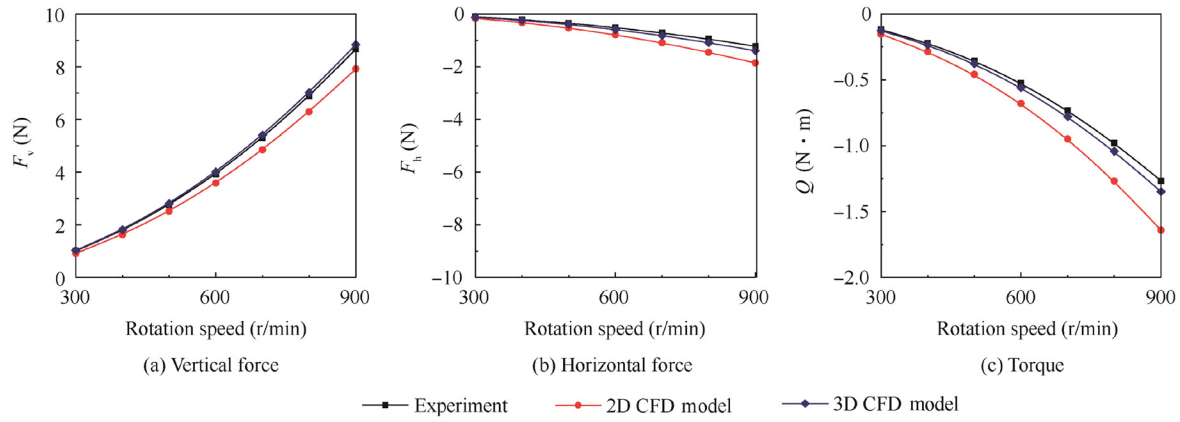


**Fig. 5** Comparison of numerical simulation results and experimental data.

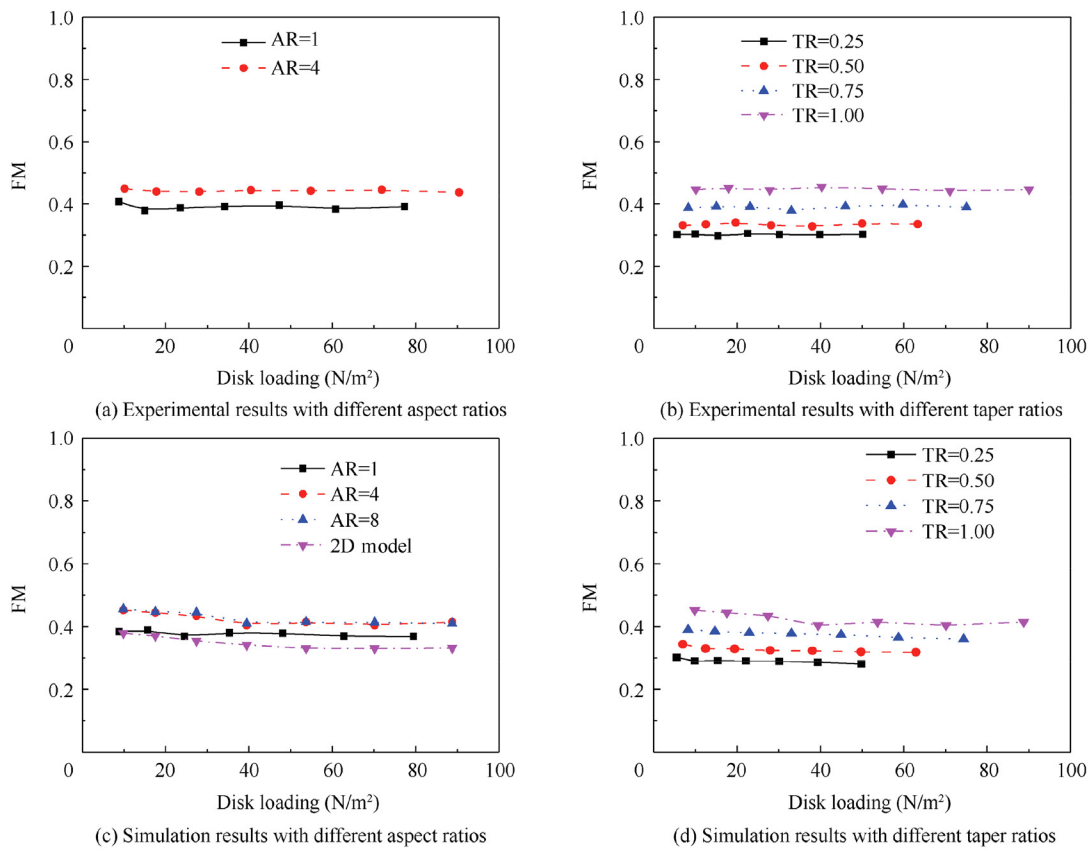


**Fig. 6** Comparison of efficiency of cycloidal rotors with different blade platforms.

**Table 2** Parameters of test cases with different blade platforms.

Parameter	Cases with different aspect ratios	Cases with different taper ratios
Rotor diameter (mm)	360	360
Number of blades	4	4
Root chord length (mm)	70	70
Blade taper ratio	1.0	0.25 (AR = 6.4), 0.5 (AR = 5.3), 0.75 (AR = 4.57), 1.0 (AR = 4)
Blade aspect ratio	1, 4, 8 and 2D model (infinite)	NACA0015
Airfoil of blade	NACA0015	NACA0015
Blade pitch axis position	50% chord length from leading edge	50% chord length from leading edge
Pitch angle amplitude (°)	±45	±45

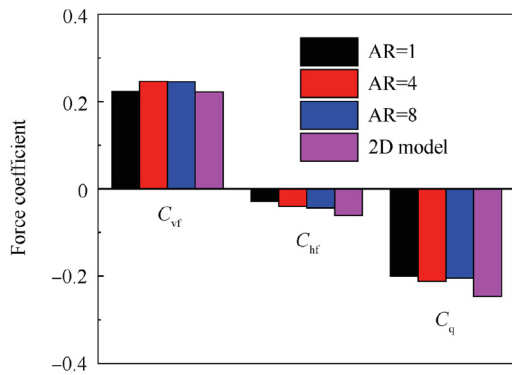


Fig. 7 Time averaged rotor force coefficients in one cycle ( $\omega = 900$  r/min).

are tested and finally it is found that 1200 steps per cycle is fine enough to produce time independent solution.<sup>1</sup>

### 3.6. Coordinate system

The analyses of all test cases are based on the inertial reference frame and the moving reference frame that rotate with the

cycloidal rotor, as shown in Fig. 4. The rotation speed of the rotor is  $\omega$  and the azimuth angle of Blade 1 and rotor is  $\theta$ .  $\theta = 0^\circ$  when Blade 1 is located at top most position of its trajectory. The rotor shaft is defined as  $Z$ -axis. The vertical force, or  $F_v$ , is along  $Y$ -axis and is positive if it points upwards. The horizontal force, or  $F_h$ , is along  $X$ -axis and it is positive if it points rightwards.  $\varphi$  is the thrust offset angle. The tangential force is along the direction of the blade tangential velocity and it is positive if it is in the same direction as the tangential velocity. The radial force is along the direction of the blade supporting strut and it is positive when it points outwards.

### 4. Validation of numerical simulation model

The results from the numerical simulation and the force measurement experiments are compared. The comparison shows that the numerical simulation can produce results that match well with the experimental data. The 3D model can produce better prediction of aerodynamic forces than the 2D model, especially the side force, as shown in Fig. 5.

The hover efficiency of the cycloidal rotors with different blade platforms is shown in Fig. 6. The hover efficiency of the rotors is measured by the Figure of Merit (FM). It is defined as the ratio of ideal power with respect to the actual

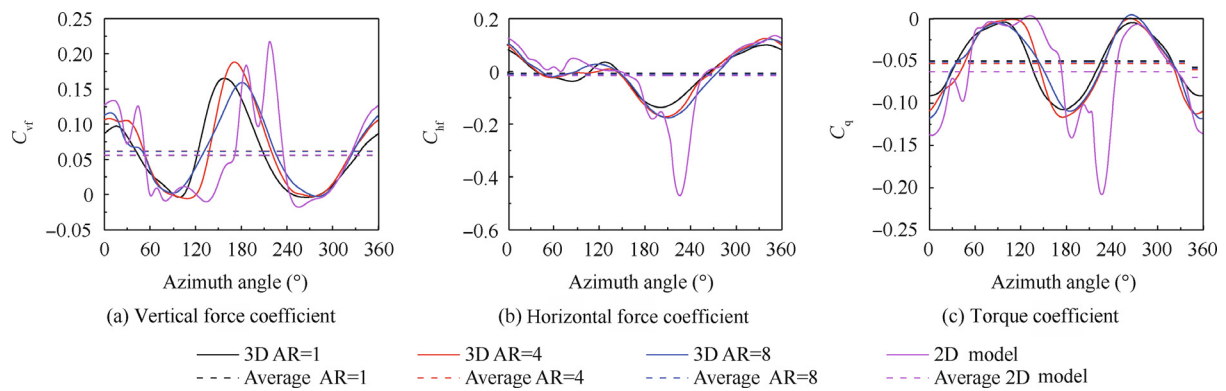


Fig. 8 Force generation history of one blade in one cycle (inertial frame,  $\omega = 900$  r/min).

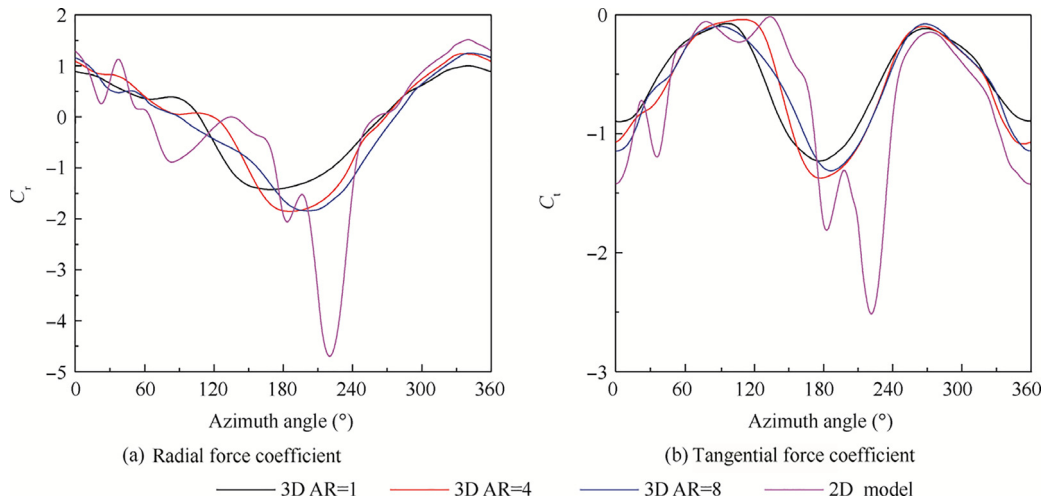


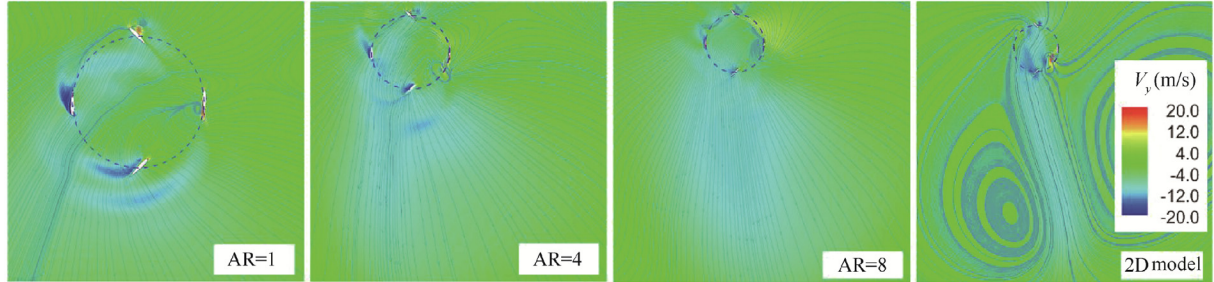
Fig. 9 Force generation history of one blade in one cycle.

power required to hover. Since the FM increases with the thrust coefficient, usually the efficiency of two rotors is compared with the same disc loading.<sup>28</sup>

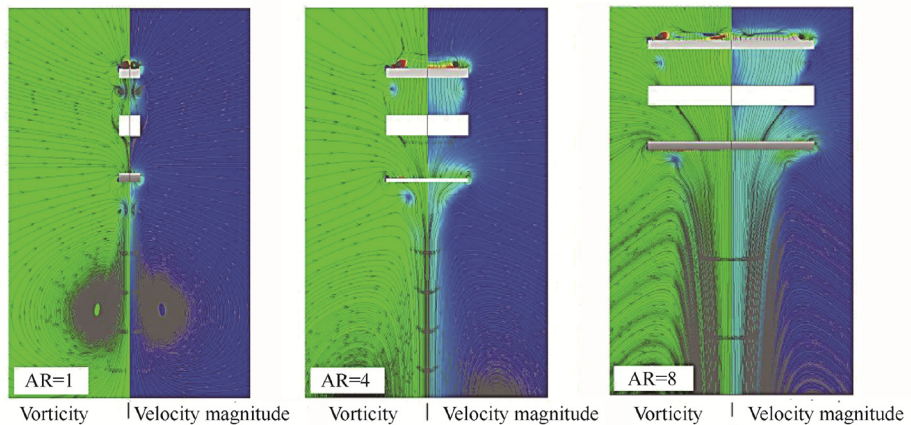
$$FM = \frac{\text{ideal power}}{\text{actual power}} = PL \sqrt{\frac{DL}{2\rho}} \quad (2)$$

where: FM is hover efficiency, PL is power loading, DL is disk loading.

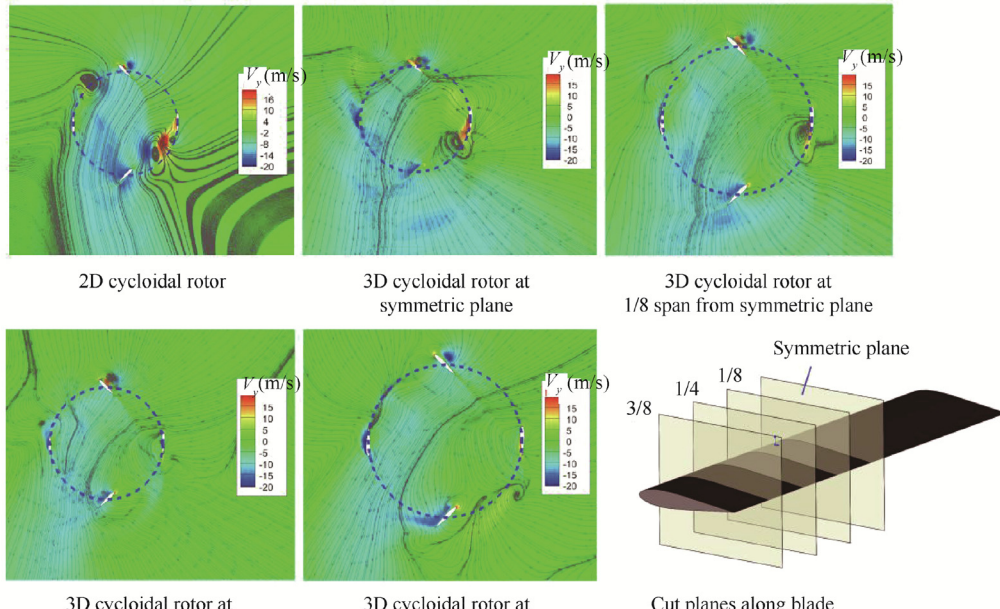
In this paper, only the cycloidal rotors working at large pitching amplitude are discussed, since the cycloidal rotors perform better when the blades are set to high pitching amplitudes.<sup>9,11</sup> The numerical simulations based on different blade



(a) Vertical velocity  $V_y$  distribution of cycloidal rotors observed in symmetric plane of rotor



(b) Vorticity and velocity magnitude of cycloidal rotors observed at  $YOZ$  plane



(c)  $V_y$  distribution at different span-wise cut planes ( $AR=4, \theta=0^\circ, \omega=900 \text{ r/min}$ )

**Fig. 10** Comparison of flow field around cycloidal rotors with different aspect ratios.

platform shapes are performed, as defined in [Table 2](#). Then the experimental results ([Fig. 6](#) (a) and (b)) are compared with the results from CFD simulations ([Fig. 6](#) (c) and (d)). In [Fig. 6](#) (a), only the experimental results for  $AR = 1$  and  $AR = 4$  are available, since the centrifugal force of the blade with high aspect ratio causes large deformation and vibration.

From the experimental results, it can be seen that the hover efficiency increases slightly with blade aspect ratio and drops with decreased taper ratio. The experimental results and numerical simulation results show the same trend of the effects of the blade platform shape. Therefore the analyses in the rest part of this paper are all based on numerical simulations.

## 5. Results and discussion

Having gained the confidence on the proposed numerical simulation model, the aerodynamic forces of cycloidal rotor with aspect ratio of 1, 4, 8 and 2D model (infinite aspect ratio) are analyzed to figure out the effects of the aspect ratio and BTVs upon the performance of the cycloidal rotor. The dimensions of the test cases are defined in [Table 2](#).

### 5.1. Cases with different aspect ratios

The FM of the cycloidal rotors with different aspect ratios is shown in [Fig. 6](#). It can be seen that the FM increases slightly with the aspect ratio. The averaged FM of  $AR = 8$  is only 14% higher than the cases with  $AR = 1$ . The FM computed from 3D numerical simulation model is slightly higher than that from 2D model. However, for the test cases with different airfoils, the FM can be improved by 40%<sup>29</sup> and for the test cases with different blade chord lengths, the FM can be improved by three fold.<sup>30</sup> Therefore the improvement of FM

due to larger aspect ratio is much less significant than that due to the airfoil and chord length.

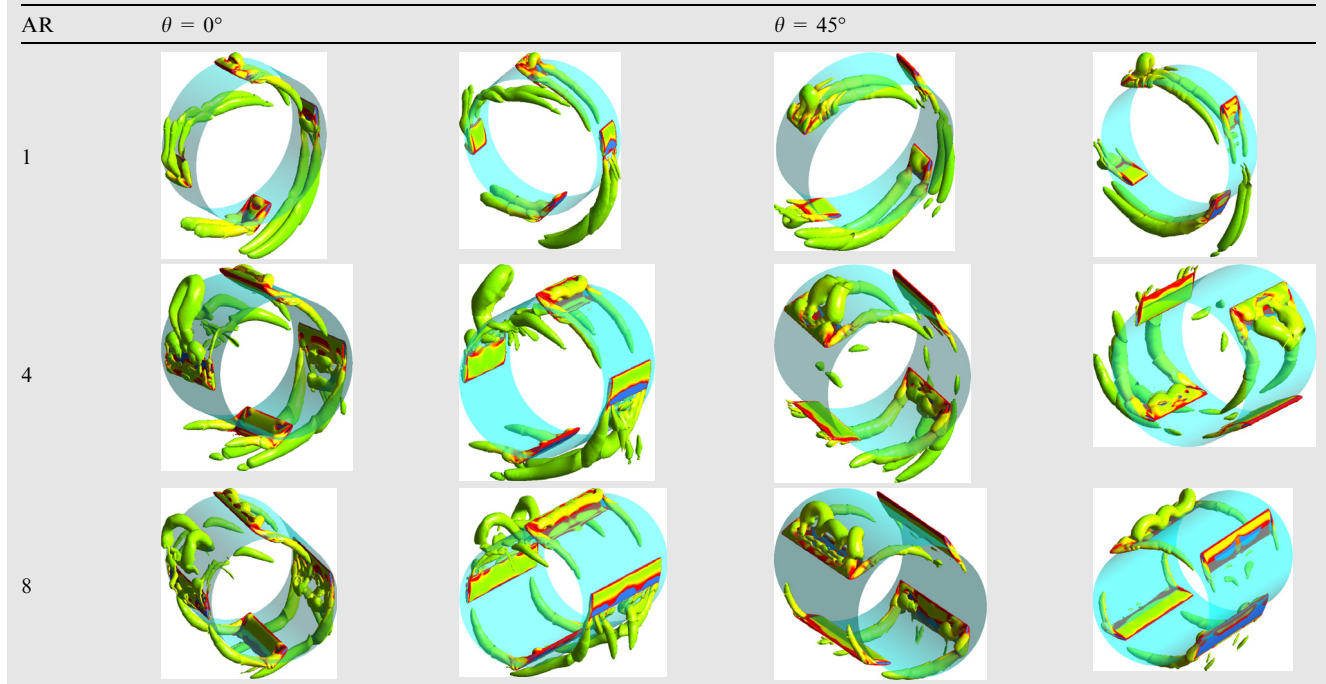
The time averaged rotor forces in one cycle are shown in [Fig. 7](#), where  $C_{vf}$  is vertical force coefficient,  $C_{hf}$  is horizontal force coefficient and  $C_q$  is torque coefficient. It can be seen that, for all 3D cases with BTVs, the aerodynamic force coefficients do not vary much with the aspect ratio. The vertical forces of 3D models are slightly higher than those of 2D model.

The aerodynamic forces of the rotors with different blade aspect ratios in one cycle are shown in [Fig. 8](#), where  $C_r$  is radial force coefficient and  $C_t$  is tangential force coefficient. The forces in the moving reference frame are shown in [Fig. 9](#). It can be seen that although the time averaged forces of the rotors with finite blade span are quite close to those obtained by 2D model, and the instantaneous forces are quite different. For the 2D cases, there are quite large force peaks. The blade pitching angle reaches maximum when the azimuth angle is  $180^\circ$ ; however the force peak is delayed and it is located at the azimuth angle around  $220^\circ\text{--}240^\circ$ . For the 3D cases, the force curves are much smoother and the aerodynamic force reaches maximum when azimuth angle is around  $180^\circ$ . The horizontal force peak and torque of the 3D cases are also much smaller than those of the 2D cases.

The velocity and vorticity distributions in inertial frame are shown in [Fig. 10](#). From [Fig. 10](#) (a), it can be seen that the larger the aspect ratio is, the more intense the downwash in the rotor cage and the slip stream are. For the cycloidal rotor with very small aspect ratio ( $AR = 1$ ), the downwash in the rotor cage is very weak. The BTVs tend to alleviate the downwash in the rotor cage and the slip stream.

The vorticity contour and span-wise velocity distribution are displayed in [Fig. 10](#)(b). There are downwash areas below

**Table 3** Vortex structure and velocity distribution as viewed from different directions. ( $Q$  criterion,  $Q = 0.001$ ).



the blades. The higher the aspect ratio is, the wider the downwash area there will be. The slip stream of the rotor is highly contracted below both the top blade and the lower blade, which means that the blades are producing thrust. This is consistent with the PIV experimental results from Ref.<sup>31</sup> The spanwise vertical velocity distribution of the cycloidal rotor with AR = 4 is shown in Fig. 10 (c). There are downwash in the rotor cage in all span-wise sections. But the center part of the blade experiences stronger downwash than the blade tip.

The vortex structures of the cycloidal rotors with different aspect ratios in one cycle are shown in Table 3. It can be seen that for all cases in this section, the pitching motion of the blade induces 3D dynamic stall. DSVs are highly distorted and the  $\Omega$  shape vortex can be clearly seen. The span-wise length of the DSVs increases with the aspect ratio and the BTVs induce strong span-wise flow and downwash upon the blade.

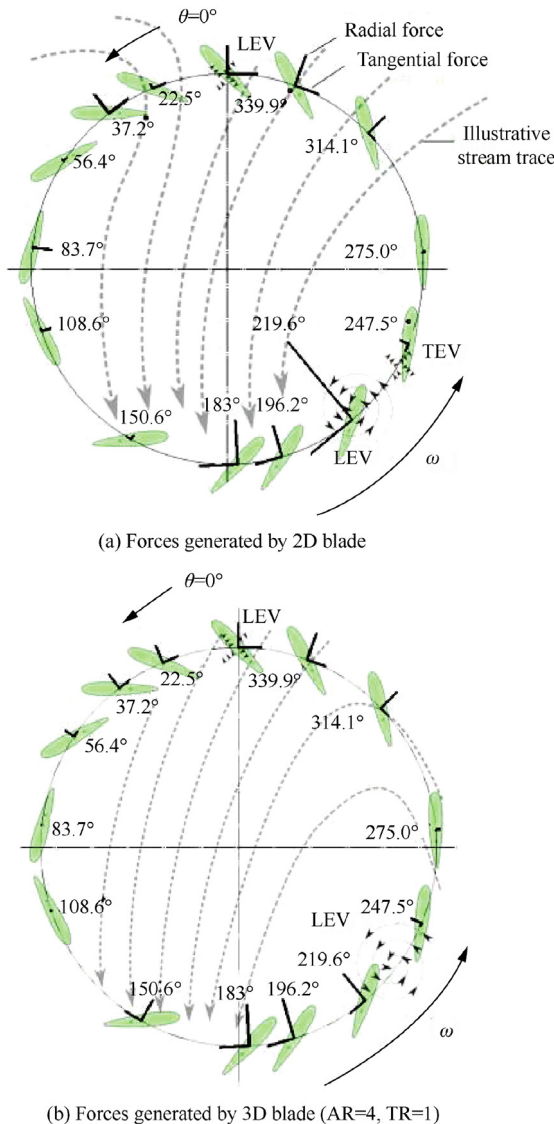


**Fig. 11** Scaled radial and tangential aerodynamic forces generated by a blade in one cycle.

### 5.2. Discussion on effects of aspect ratio

The flow field of cycloidal rotor at symmetric plane observed in inertial frame is shown in Fig. 10(c) and Fig. 11. The flow field at symmetric plane observed in moving frame is shown in Fig. 12. There are DSVs and downwash in the rotor cage of both 2D and 3D cycloidal rotors. The downwash reduces the effective AOA of the blade when blade is traveling through the lowest point of its trace. Hence no DSV is observed when the blade pitch angle reaches maximum. The 2D cycloidal rotor and 3D cycloidal rotor have quite similar aerodynamic forces and vorticity contour when the blade is located at the upper part of its trace. The major differences occur when the blade is located at the lower part of its trace. This is due to the fact that the 2D cycloidal rotor has much stronger downwash in the right part of the rotor cage than the 3D cycloidal rotor, as shown in Fig. 10(a) and Fig. 11. For the 2D case, when the blade passes through the lowest point of its trace, the strong downwash increases the inflow velocity experienced

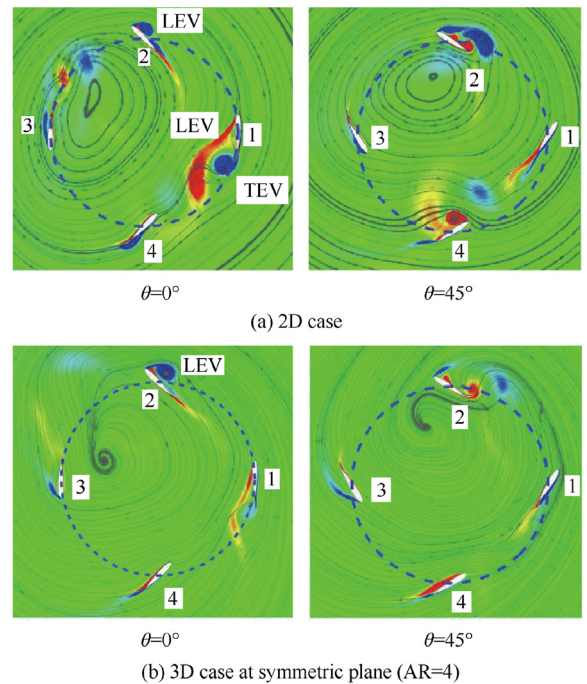


**Fig. 12** Flow field of cycloidal rotor observed at symmetric plane in moving frame.

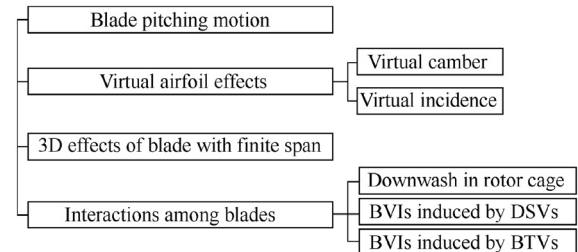


**Fig. 13** Primary influencing factors upon aerodynamic forces of cycloidal rotors.

by the blade. At the same time, there are strong parallel BVIs induced by the Leading Edge Vortex (LEV) and Trailing Edge Vortex (TEV) from the preceding blade (Fig. 12 (a),  $\theta = 45^\circ$ , Blade 4), and thus there are strong force peaks when the blade is located at the lower right part of its trace.<sup>1,18</sup> This is the major source of very large horizontal force peak and torque peak in the 2D model. For the 3D cycloidal rotor, the BTVs tend to diminish the downwash in the right part of the rotor cage. There is no increased inflow velocity or BVI induced by DSVs (Fig. 12(b),  $\theta = 45^\circ$ , Blade 4). Therefore 3D cycloidal rotor has much smoother force curve, and smaller horizontal force and torque peaks.<sup>1</sup>

The aerodynamic forces of cycloidal rotors are influenced by pitching motion of the blade, the virtual airfoil effects of the blade, the effects of BTVs, the interactions among the blades and the effects of viscosity. The interactions among the blades primarily involve the downwash in the rotor cage and the BVIs induced by DSVs and BTVs, as shown in Fig. 13. According to previous research, it is found that due to relatively high reduced frequency, the aerodynamic forces due to viscosity are very small in comparison with the forces due to pressure.<sup>32</sup>

For the 3D cases discussed in this section, it can be seen that the BTVs make the DSVs highly distorted and no significant parallel BVI induced by DSVs can be observed.<sup>1</sup> The BTVs also can induce the perpendicular BVIs and change the intensity of the downwash in the rotor cage. However, although these cases have quite different aspect ratios, they have quite similar FM and force generation history. The effects of BTVs and downwash do not have significant impact on the performance of the cycloidal rotors. Hence we can reach the conclusion that the time averaged aerodynamic forces of

the cycloidal rotors with very large pitching amplitude are primarily affected by the unsteady aerodynamic effects due to blade pitching motion.

### 5.3. Effects of taper ratio at large pitching amplitude

Another important parameter of the blade platform is the taper ratio. In order to understand the effects of the taper ratio, three numerical simulation models listed below are developed and the results of them are compared against each other (Fig. 14).

- (1) The first model is based on blade element theory so that the blade is divided into a number of blade elements. The CFD simulations using 2D model with different blade chord lengths are carried out, and then the aerodynamic forces of the rotor are integrated along blade span based on the blade element forces. This model does not consider the effects of BTVs and is denoted as Blade Element Method (BEM) model (Fig. 14 (a)).
- (2) The second is the CFD simulation model based on 2D rotors that shares the same Mean Aerodynamic Chord (MAC) length as the 3D model, and the equivalent blade platform is assumed to be a rectangle. The aerodynamic forces are then integrated along blade span. This model also does not consider the effects of BTVs and is denoted as Equivalent MAC (EM) model (Fig. 14 (b)).
- (3) The third model is the full 3D CFD simulation model that involves the effects of the DSVs and BTVs. This model is denoted as 3D model (Fig. 14 (c)).

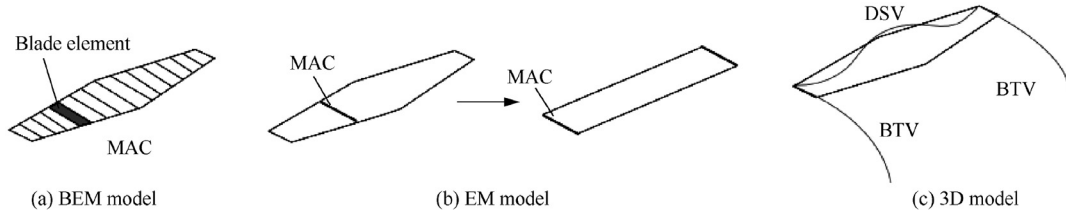


**Fig. 14** Numerical simulation models for cycloidal rotors with different taper ratios.

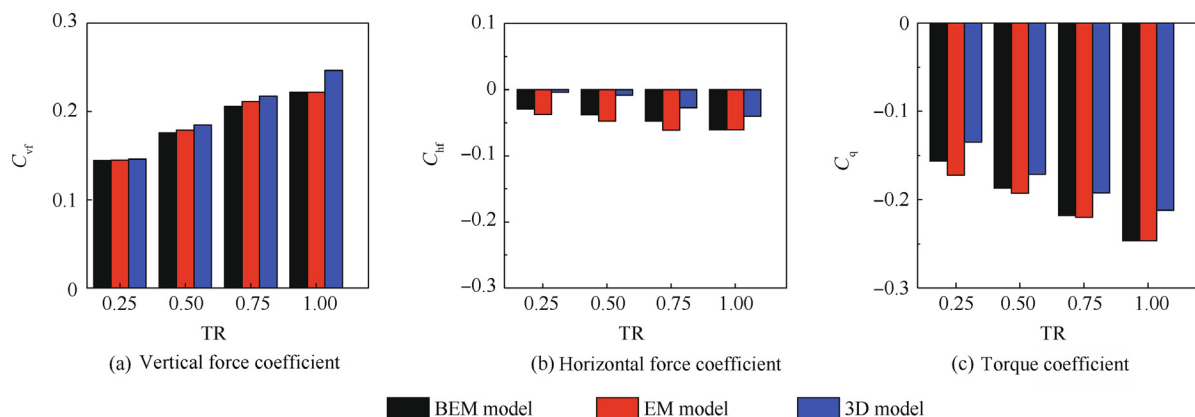


**Fig. 15** Time averaged aerodynamic forces of cycloidal rotors with different taper ratios.

#### 5.4. Cases with different taper ratios

The comparison of the time averaged rotor forces is shown in Fig. 15 and the comparison of FM is shown in Fig. 6. For the test cases in Fig. 15, all blades share the same span and root chord length but different tip chord lengths. The forces of cycloidal rotors increase with taper ratio. The blades with smaller taper ratio have slightly larger aspect ratio. Therefore

according to the wing theory, it is expected that the cycloidal rotors with taper ratio near 0.4 and 0.5 would be more efficient.<sup>33</sup> However in Fig. 6, the FM increases with taper ratio.

The instantaneous aerodynamic forces produced by one blade in one cycle are shown in Fig. 16. When TR = 1, the BEM model produces the same blade forces as the EM model. It can be seen that although the BTVs do not influence the time averaged forces of the cycloidal rotor, they change the instan-

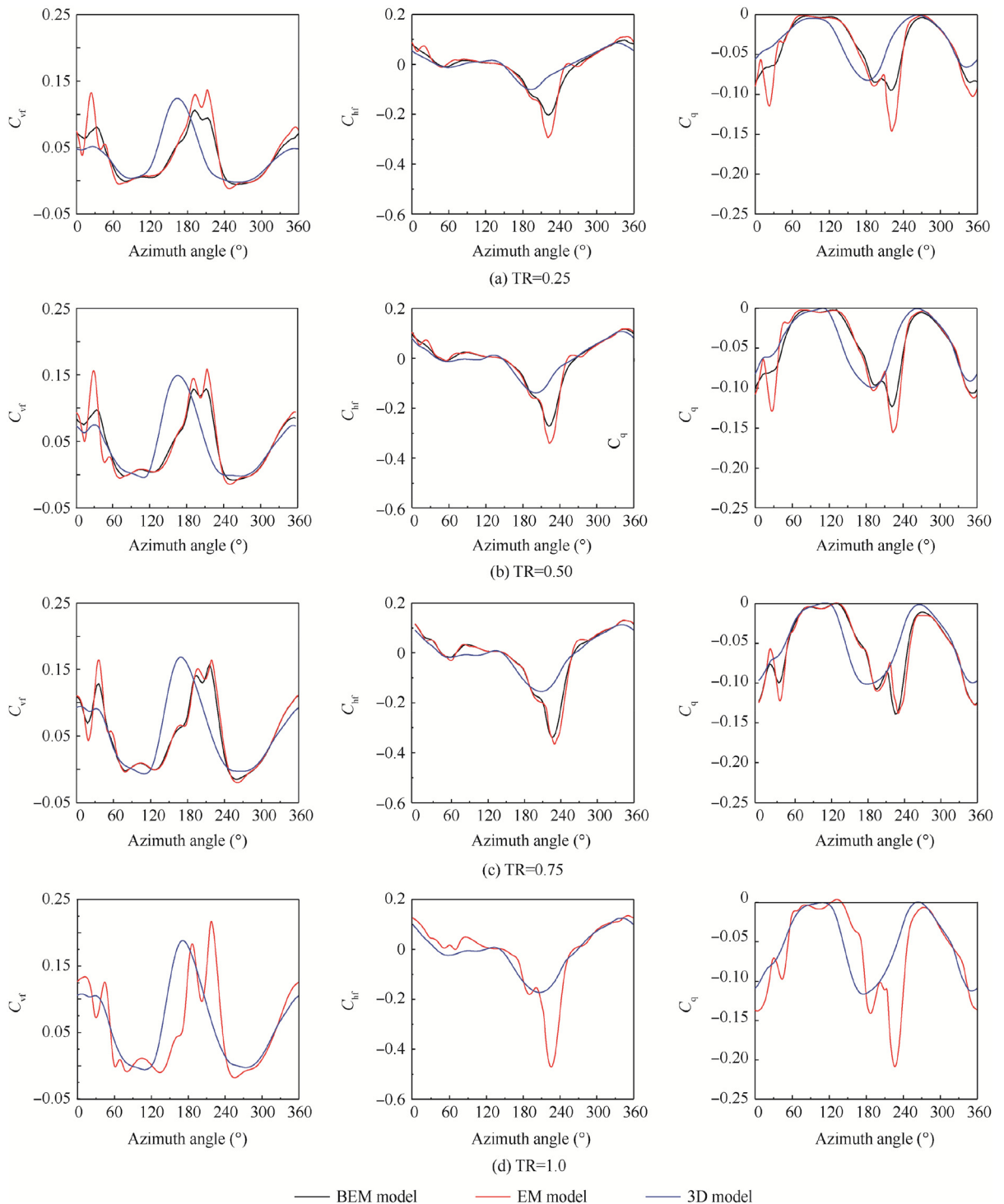


**Fig. 16** Force generation history of one blade in one cycle obtained by different simulation models.

taneous aerodynamic forces of the rotor. The BTVs make the dynamic stall smoother than the predicted 2D models. This is the same as the test cases with different aspect ratios.

The downwash velocity distributions at the mid-span plane and the  $Y\text{O}Z$  plane are shown in Fig. 17. It can be seen that the taper ratio does not significantly change the downwash in the rotor cage. The test cases have quite similar downwash velocity distribution in the rotor cage.

### 5.5. Discussion on effects of taper ratio

The instantaneous forces of the 2D cycloidal rotor blade with different chord lengths are shown in Fig. 18. Since the rotors with larger  $C/R$  have higher reduced frequency, the time interval of positive tangential force is wider and the magnitude of the positive tangential force is larger. Positive tangential force reduces the time averaged torque as well as the power of the cycloidal rotor.<sup>30</sup> However, if the  $C/R$  is greater than 0.6, there

is very large negative vertical force due to very strong downwash in the rotor cage.<sup>30</sup> In this case, the efficiency of the rotor drops. For the test cases defined in Table 2, the highest  $C/R$  is 0.38. The larger the taper ratio is, the closer the  $C/R$  is to 0.5; therefore the rotor with larger taper ratio has better efficiency in hover.

From Fig. 15, it also can be seen that for the same taper ratio, results from BEM and EM model match each other well. All three models produce quite similar time averaged vertical force and torque except the horizontal force. This confirms that the 3D effects play a secondary role on time averaged aerodynamic forces.

According to Spentzos et al., if the blade reduced frequency is high, the motion of the body dominates.<sup>27</sup> For the blade of cycloidal rotor, the reduced frequency is defined as

$$\kappa = \frac{\omega C}{2V_t} = \frac{\omega C}{2\omega R} = \frac{C}{2R} \quad (3)$$

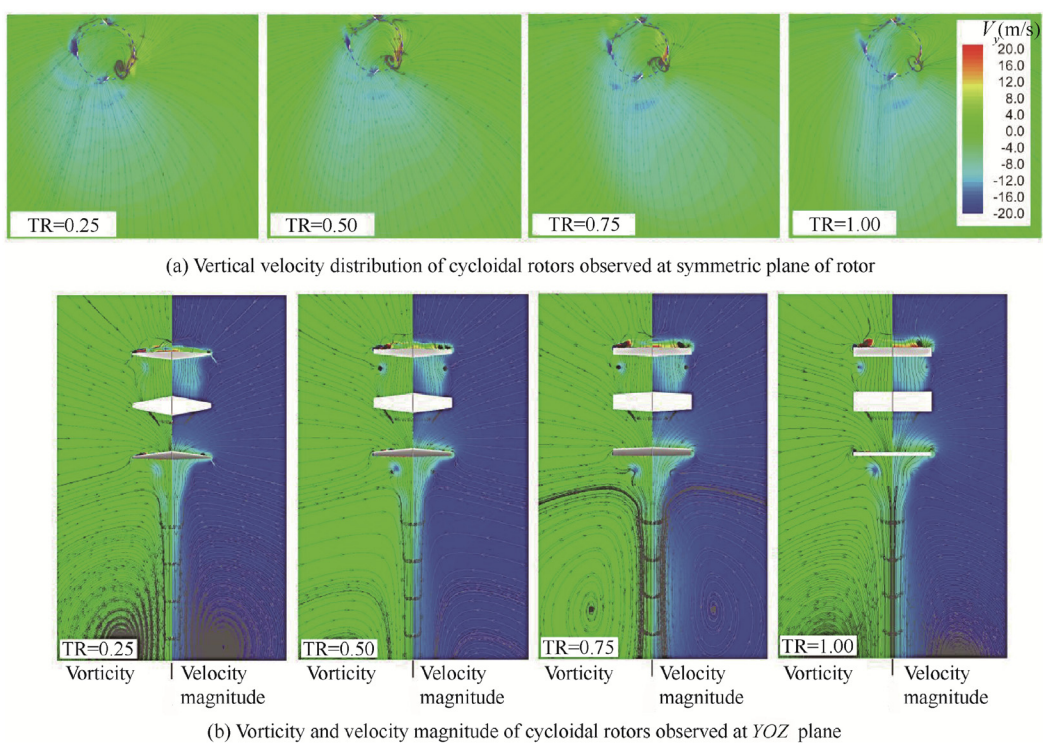


**Fig. 17** Velocity distribution of cycloidal rotors with different taper ratios.

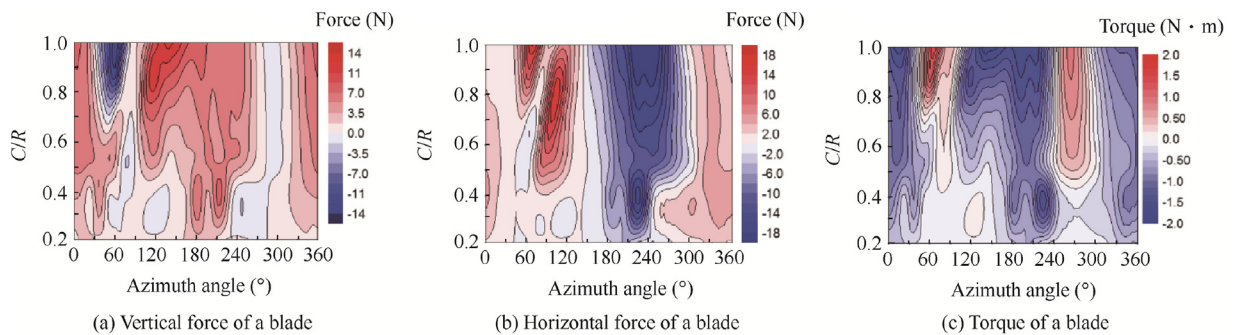


**Fig. 18** Instantaneous blade forces with different airfoil chord lengths (2D model,  $\omega = 900$  r/min, NACA0015).

where  $\kappa$  is reduced frequency,  $C$  is blade chord length,  $V_t$  is tangential velocity of the blade and  $R$  is rotor radius.

Since the frequency of the blade oscillation equals the frequency of rotor rotation, the reduced frequency of the cycloidal rotor blade is determined by chord to radius ratio. For the cases discussed in this paper, the reduced frequency ranges from 0.12 to 0.2, which means that the blade of cycloidal rotor is working at relatively high reduced frequency. This might be the reason why the efficiency of the cycloidal rotor is primarily affected by unsteady blade motion.

## 6. Conclusions

In this paper, the effects of the aspect ratio and taper ratio on the cycloidal rotor working at large pitching amplitude are analyzed using the URANS solver. The blade kinetics is derived and incorporated into the solver with the help of UDFs. The sliding mesh schemes for both 2D and 3D cycloidal rotors are presented in this paper. The results from simulation models with and without blade tip vortices are compared and analyzed. The analysis results can provide a qualitative guidance for designing blade platform of the cycloidal rotors. The range of the analyses is limited to large blade pitching amplitude considering the fact that cycloidal rotors work best at large pitching amplitude.

The following conclusions are drawn based on the above analysis:

- (1) The downwash in the rotor cage changes according to the variation of the blade aspect ratio. The larger the aspect ratio is, the more intense and concentrated the downwash will be. The hover efficiency of the cycloidal rotor increases slightly with aspect ratio. However, compared with the blade airfoil and chord length, the efficiency does not change significantly with aspect ratio, although the aspect ratio varies from a very small value to a large one.
- (2) The FM increases slightly with the taper ratio. Among the cycloidal rotors discussed in this paper, the one with taper ratio equal to unity is the most efficient. This is due to the reason that the FM increases with the blade chord length when the  $C/R$  is smaller than 0.5. The larger the taper ratio is, the closer the  $C/R$  approaches 0.5.
- (3) The DSVs due to 3D dynamic stall can be observed since the cycloidal rotors work at large pitching amplitude. The BTVs partially diminish the downwash in the rotor cage. This leads to smaller torque and horizontal force compared with the 2D counterpart.
- (4) When the blade pitching amplitude is large, the effects of the aspect ratio and taper ratio on the hover efficiency do not follow the wing theory for fixed wing aircraft. The 3D effects of blades do not have major impact on the efficiency of the cycloidal rotors. This shows that the unsteady aerodynamic effects due to the blade pitching motion play a more important role in the hover efficiency than the blade platform shape. Therefore we should pay more attention to the blade airfoil and pitching motion, rather than the blade platform shape.

## References

1. Hu Y, Zhang HL, Wang GQ. Two dimensional and three dimensional numerical simulation of cycloidal propellers in hovering status. *54th AIAA aerospace science meeting*. Reston: AIAA; 2016.
2. Benedict M, Mattaboni M, Chopra I, Masarati P. Aeroelastic analysis of a micro-air-vehicle-scale cycloidal rotor in hover. *AIAA J* 2011;49(11):2430–43.
3. Benedict M, Chopra I, Ramasamy M, Leishman JG. Experimental investigation of the cycloidal-rotor concept for a hovering micro air vehicle. American Helicopter Society 64th Annual Forum. 2008. p. 1071–92.
4. Iosilevskii G, Levy Y. Experimental and numerical study of cyclogiro aerodynamics. *AIAA J* 2006;44(12):2866–70.
5. Hwang IS, Min SY, Lee CH, Kim SJ. Development of a four-rotor cyclocopter. *J Aircr* 2008;45(6):2151–7.
6. Hwang IS, Min SY, Kim MK, Kim SJ. Multidisciplinary optimal design of cyclocopter blade system. *46th AIAA/ASME/ASCE/AHS/ASC Structures and Structural Dynamics and Materials Conference*. Reston: AIAA; 2005.
7. Hwang IS, Hwang CS, Kim SJ. Structural design of cyclocopter blade system. *46th AIAA/ASME/ASCE/AHS/ASC Struct. Struct. Dyn. Mater. Conf.*. Reston: AIAA; 2005.
8. Lee CH, Yong MS, Lee JW, Kim SJ. Design, analysis, and experimental investigation of a cyclocopter with two rotors. *J Aircr* 2016;53(5):1527–37.
9. Benedict M, Ramasamy M, Chopra I. Improving the aerodynamic performance of micro-air-vehicle-scale cycloidal rotor: An experimental approach. *J Aircr* 2010;47(4):1117–25.
10. Benedict M, Jarugumilli T, Chopra I. Effect of rotor geometry and blade kinematics on cycloidal rotor hover performance. *J Aircr* 2013;50(5):1340–52.
11. Benedict M, Shrestha E, Hrishikeshavan V, Chopra I. Development of a micro twin-rotor cyclocopter capable of autonomous hover. *J Aircr* 2014;51(2):672–6.
12. Zhao QJ, Ma YY, Zhao GQ. Parametric analyses on dynamic stall control of rotor airfoil via synthetic jet. *Chin J Aeronaut* 2017;30(6):1818–34.
13. Wang YB, Qin N, Zhao N. Delaunay graph-based moving mesh method with damping functions. *Chin J Aeronaut* 2018;31(11):2093–103.
14. Yang K. Aerodynamic analysis of an mav-scale cycloidal rotor system using a structured overset rans solver [dissertation]. Maryland: University of Maryland; 2010.
15. Leger JA, Passcoa JC, Xisto CM. Analytical modeling of a cyclorotor in hovering state. *Proc Inst Mech Eng Part G J Aerosp Eng* 2015;229(12):2163–77.
16. Xisto C, Leger J, Pascoa J, et al. Parametric analysis of a large-scale cycloidal rotor in hovering conditions. *J Aerosp Eng* 2017;30(1), 04016066-1–14.
17. Gagnon L, Morandini M, Quaranta G, Muscarello V, Masarati P. Aerodynamic models for cycloidal rotor analysis. *Aircr Eng Aerosp Technol* 2016;88(2):215–31.
18. Hu Y, Du F, Zhang HL. Investigation of unsteady aerodynamics effects in cycloidal rotor using RANS solver. *Aeronaut J* 2016;120(1228):956–70.
19. McNabb ML. Development of a cycloidal propulsion computer model and comparison with experiment. *Sci Total Environ* 2014;488–489(1):26–35.
20. Tang J, Hu Y, Song BF, Yang H. An unsteady free wake model for aerodynamic performance of cycloidal propellers. *Proc IMechE Part G J Aerosp Eng* 2016;232(2):290–307.
21. Katz J, Plotkin A. Low-speed aerodynamics, second. edition. Cambridge: Cambridge University Press; 2001.p.183..

22. Prabhu JJ, Nagarajan V, Sunny MR. On the fluid structure interaction of a marine cycloidal propeller. *Appl Ocean Res* 2017;64:105–27.
23. Norton Robert L *Design of machinery: An introduction to the synthesis and analysis of mechanisms and machines*. McGraw-Hill Science/Engineering/Math.; 2003. p. 144–67.
24. Mcnaughton J, Billard F, Revell A. Turbulence modelling of low Reynolds number flow effects around a vertical axis turbine at a range of tip-speed ratios. *J Fluids Struct* 2014;47(5):124–38.
25. Wang SY, Ingham D B, Ma L, Pourkashanian M, Tao Z. Numerical investigations on dynamic stall of low Reynolds number flow around oscillating airfoils. *Comput Fluids* 2010;39:1529–41.
26. Nobile R, Vahdati M, Barlow J, Mewburn-Crook A. Dynamic stall for a vertical axis wind turbine in a two-dimensional study. 2011 world renewable energy congress. 2011. p. 4225–32.
27. Spentzos A, Barakos G, Badcock K, et al. Investigation of three-dimensional dynamic stall using computational fluid dynamics. *AIAA J* 2005;43(5):1023–33.
28. Pereira JL. Hover and wind-tunnel testing of shrouded rotors for improved micro air vehicle design [dissertation]. Maryland: University of Maryland; 2008.
29. Hu Y, Zhang HL, Tan C. The effect of the aerofoil thickness on the performance of the MAV scale cycloidal rotor. *Aeronaut J* 2015;119(1213):343–64.
30. Hu Y, Zhang HL. The effect of the blade chord length on the aerodynamics of the MAV scale cycloidal propeller under hovering status. *45th AIAA Fluid Dynamic Conference*. Reston: AIAA; 2015.
31. Benedict M. *Fundamental understanding of the cycloidal-rotor concept for micro air vehicle applications* [dissertation]. Maryland: University of Maryland; 2010.
32. Hu Y, Zhang HL, Wang GQ. The effects of dynamic-stall and parallel BVI on cycloidal rotor. *Aircr Eng Aerosp Technol* 2017;90(1):87–95.
33. Raymer Daniel P. *Aircraft design: a conceptual approach*. fourth edition. Reston: AIAA; 2006.